Journal of Magnetism and Magnetic Materials 547 (2022) 168889

Contents lists available at ScienceDirect

Journal of Magnetism and Magnetic Materials

journal homepage: www.elsevier.com/locate/jmmm

Particle motion artifacts in equilibrium magnetization measurements of large iron oxide nanoparticles

Shehaab Savliwala [a], Sitong Liu (刘思彤) [b], Carlos M. Rinaldi-Ramos [c,d,*]

[a] Department of Chemical Engineering, University of Florida, Gainesville FL-32611, United States of America
[b] Department of Chemical Engineering, University of Florida, Gainesville FL-32611, United States of America
[c] Department of Chemical Engineering, University of Florida, Gainesville FL-32611, United States of America
[d] J. Crayton Pruitt Family Department of Biomedical Engineering, University of Florida, Gainesville FL-32611, United States of America

ARTICLE INFO

Keywords:
Iron oxide nanoparticles
Superparamagnetic behavior
Langevin behavior
Equilibrium magnetization measurements
Magnetogranulometric analysis

ABSTRACT

Iron oxide nanoparticles find many applications due to their response when subjected to externally applied magnetic fields. Equilibrium magnetization measurements (commonly known as magnetization curves) are an essential characterization tool to evaluate if particles display hysteresis, and to obtain magnetic properties such as the saturation magnetization. For superparamagnetic particles, one can obtain a magnetic size distribution by fitting the data to a theoretical model, such as the Langevin function, in what is called magnetogranulometric analysis. If one wishes to use the resulting size estimates as a predictor of particle performance in applications, magnetization data must be obtained under conditions that capture the response of the particles with minimal artifacts. In this paper, we used selected iron oxide nanoparticle batches with physical size ranging from 20 to 45 nm to demonstrate the influence of sample preparation methods on the magnetization data obtained. We show that measurements in powder form and in liquid solvents display varying degrees of particle interaction artifacts at low fields, depending strongly on particle size and on the thickness of the surface coating. In addition, measurements in 'solid' waxy hydrocarbon matrices are shown to be susceptible to particle rotation artifacts for large particle sizes. Hard crosslinked polymer matrices are shown to restrict particle motion completely, resulting in magnetization data that follows the Langevin function if the measurement is performed above the blocking temperature of the particles. We end with a discussion of how the presence of matrix-dependent measurement artifacts influence the magnetic diameter fits obtained using magnetogranulometry, and how measuring above and below the blocking temperature can affect fit results.

1. Introduction

Magnetization as a function of applied magnetic field (M−H) measurements are the most commonly used technique for evaluating superparamagnetic behavior in magnetic nanoparticles and are ubiquitous in the iron oxide nanoparticle synthesis literature. For superparamagnetic particles, one can estimate the magnetic diameter distribution, an important metric that correlates to the phase purity of the nanoparticles when compared to the physical size distribution. Several theoretical models exist that allow interpretation of these measurements to extract a range of particle magnetic properties. Pioneering work by Einstein [1], Langevin [2,3], and Smoluchowski [4] defines the basic relationships used today to understand the magnetization dynamics of nanoparticle ensembles. Other seminal contributions by Kittel [5], Néel [6], Stoner-Wohlfarth [7], Brown [8,9], Fokker-Planck [10], Kolmogoroff [11], and Landau, Lifshitz and Gilbert [12,13] provide frameworks for interpretation of single-domain and multidomain ferromagnetic nanoparticle behavior. These models are simple but elegant, and their utility lies in the fact that they are general enough for others to adapt based on the specific details of the particle systems and data being studied.

As progress in the field of nanoparticle synthesis took place, several groups began to obtain data that deviated from the predictions offered by these models. To a large extent, work on the refinement of models mentioned above has been driven by the need for theories to explain real-world magnetization characteristics of metal and metal-oxide nanoparticles with an overwhelmingly wide range of physical and magnetic properties. Notable among contributions before the turn of the

* Corresponding author.
E-mail addresses: s.savliwala@ufl.edu (S. Savliwala), liusitong@ufl.edu (S. Liu (刘思彤)), carlos.rinaldi@ufl.edu (C.M. Rinaldi-Ramos).

https://doi.org/10.1016/j.jmmm.2021.168889
Received 20 April 2021; Received in revised form 2 October 2021; Accepted 24 November 2021
Available online 29 November 2021

century are the works of Vogel and Fulcher [14–16], who accounted for contributions of inter-particle interactions to magnetization curves in non-dilute particle systems, Akulov [17,18] for their approach to saturation model for single crystal particles, Bean, Livingston and Jacobs [19,20], who account for change in domain magnetization as a function of particle size and the presence of multiple domains within a particle, Johnson [21], who accounted for the presence of multiple contributions to particle anisotropy, Berkowitz and coworkers [22] for dead layer theory, Kaiser and Miskolczy [23] for a model that incorporates a non-magnetic surface shell (commonly known in current literature as the magnetically dead layer or disordered layer), Chantrell [24] and O'Grady [25], who incorporated a lognormal or gaussian magnetic size distribution respectively into the stochastic Langevin function, Pfeiffer [26,27] for incorporation of thermal fluctuations into the Stoner-Wohlfarth model, Chen [28,29] for the concept of demagnetizing factors for non-spherical particles as a function of measurement temperature and particle concentration, Stearns and Cheng [30], who accounted for the presence of superparamagnetic and ferromagnetic contributions to the magnetization of a system of core–shell particles, Respaud [31] for a methodology accounting for surface effects in ultrafine particles, and Allia and coworkers [32,33], who account for dipolar interactions in hysteretic systems. Over the past two decades, due to increased access to high-performance processors and parallel computing, this body of work has also been heavily supplemented by computational and theoretical work modeling magnetization dynamics of magnetic nanoparticles [34–49]. There are many more individual contributions than we can cite here; instead, we refer the interested reader to comprehensive reviews that cover recent advances in the field in much greater detail [50–58].

Having provided a summary of the theoretical framework for interpretation of magnetization measurements, we pivot to the measurements themselves. Equilibrium magnetization measurements are commonly done with the dried nanoparticles as a powder [47,59–62], but it has already been shown in literature that this produces measurements that align with predictions from models only in very limited cases. In most situations, close contact and interactions between the particles as a powder influence the measured magnetization [60,62]. Besides powder measurements, the other common format of performing these measurements is with the nanoparticles suspended in a liquid solvent [63–74]. The rationale behind this lies in the idea that the ability to freely rotate and maintain random orientation distribution in a liquid allows otherwise ferromagnetic particles to behave as superparamagnets even below their blocking temperature. This concept was first discussed by Shliomis [75,76], who coined the term "extrinsic superparamagnetism" for ferrofluids that display this behavior. However, just as with measurements in nanoparticle powders, the presence of inter-particle interactions and the introduction of complexity in particle structure or composition can affect these measurements as well.

In this work, we use selected iron oxide nanoparticle batches in the 20–45 nm size range, synthesized in our lab via modifications to previously published methods [72,77] to investigate the effect of sample preparation methods on magnetization measurements. Measurements with powder samples were used to confirm the presence of particle motion and close contact artifacts in the low-field region (±10 mT) of magnetization curves, which would prevent reliable interpretation of the data unless one accounted for the contribution of interactions to the response. Next, we demonstrate that deviations from superparamagnetic behavior appear at low fields even at dilute particle concentrations in low viscosity liquid solvents such as toluene, and that the Langevin function weighted with a magnetic diameter distribution for the nanoparticles fails to capture the measured magnetic behavior. In other words, the particle suspensions displayed "non-Langevin behavior". We further show that the same particles, when prevented from coming into close contact by the replacement of their thin oleic acid surface coatings with a thicker brush-like polyethylene glycol coating, exhibited a magnetic response that conforms to a magnetic size distribution-weighted Langevin function. In the context of this manuscript, we henceforth call this "Langevin behavior". Next, measurements of the same nanoparticle samples embedded in long-chain hydrocarbons (docosane and hexatriacontane) that would be considered "hard waxy solids" at room temperature were performed to test whether suppressing physical translation of particles would lead to elimination of the non-Langevin behavior in magnetization. Instead, we observed magnetic behavior that suggests that the entire ensemble of particles undergoes rapid magnetization reversal when the field changes direction, causing extreme deviations from Langevin behavior close to zero field. Lastly, we show that immobilization in a hyper-crosslinked microporous polymer matrix such as polystyrene-divinyl benzene (PSDVB) [73,78,79]. restricts rotation as well as translation of large particles and results in magnetization data that follows Langevin behavior, if the measurement is performed at dilute particle concentrations above the blocking temperature of the particles. In those cases, measured data can be fit reliably to obtain magnetic diameter distributions using the Langevin function.

We note that the aim of this manuscript is to highlight the need for careful evaluation of the methods used to prepare magnetic nanoparticle samples for magnetization measurements, especially as particles become large. It is already well-established that the physical size and morphology of the particles, synthesis route, and the resulting magnetic properties can result in a range of complex magnetization dynamics for nanoparticle samples. Here, the effect of sample preparation methods, specifically the medium of suspension and the thickness of particle coatings, on artifacts in the measured magnetization is explored across a range of particle sizes synthesized using similar chemistry. As such, we do not attempt to evaluate if any of the several models highlighted in our opening paragraphs would allow interpretation of the non-Langevin behavior present in our data. Instead, we present it as a cautionary tale for fellow researchers. In cases where magnetogranulometry using the Langevin function is appropriate considering the behavior of particle samples, lognormal magnetic diameter fits are discussed, and an analysis of the temperature dependence of magnetic diameter estimates is presented.

2. Methods

2.1. Materials

Iron (III) acetylacetonate (99%,TCI America), oleic acid (90%, Sigma Aldrich), 1-octadecene (90%, Sigma Aldrich), docosane (99%, Sigma Aldrich), toluene (99%, Fisher Chemicals), ethanol (99%, Fisher Chemicals), 20% oxygen-argon mixture (Airgas), argon (Ultra high purity, Airgas), styrene (99%, Sigma Aldrich), azobisisobutyronitrile (AIBN, 99%, Sigma Aldrich), divinyl benzene (99%, Sigma Aldrich), hexatriacontane (99%, Acros Organics), poly(ethylene glycol) monomethyl ether (mPEG, 5 kDa, Sigma Aldrich), isopropanol (99.5%, Fisher Chemicals), acetone (99.5%, Fisher Chemicals), chromium trioxide (98%, Fisher Chemicals), sulfuric acid (99.99%, Sigma-Aldrich), hydrochloric acid (37.5% in water, Sigma Aldrich), dichloromethane (99.6%, Fisher Chemicals), diethyl ether(99%, Fisher Chemicals), 3-aminopropyltriethoxysilane (APTES, 98%, TCI America), Invitrogen™ CBQCA protein quantification kit (Fisher Chemicals), 1-Ethyl-3-(3-dimethylaminopropyl) carbodiimide (EDC, Fisher Chemicals) N-hydroxysulfosuccinimide (Sulfo-NHS, Fisher Chemicals), magnetic columns (Miltenyi Biotec) and a standard palladium sample (Quantum Design) were all obtained from specified manufacturers and used without further processing.

2.2. Particle synthesis and physical size characterization

All nanoparticles used in this study were synthesized in our lab using modifications to previously published methods [72,77,80]. Briefly, a stoichiometrically defined iron oleate precursor was synthesized by the displacement reaction of oleic acid with iron (III) acetylacetonate in a carefully controlled temperature ramp in a batch process under reflux

[81]. The iron oleate precursor was then diluted in 1-octadecene and dripped continuously into a semi-batch reactor immersed in a molten metal bath at 350 °C with an initial charge of docosane and oleic acid to act as reaction solvents. The concentration of oleic acid in the reactor varied between 0.2 M−1.1 M across the syntheses. Continuous stirring at 350 rpm was maintained using an overhead stirrer and gas infusion was controlled using a combination of mass flow controllers and needles. The final size of nanoparticles was determined by the total reaction time (ranging from 4 to 6 h), corresponding to the time after the precursor drip was initiated. One batch was synthesized in an inert argon atmosphere. Two batches were synthesized by bubbling a 20% oxygen-argon mixture into the reaction mixture. Another two batches were synthesized by adding a 1% or 5% oxygen-argon mixture to the reactor headspace, one of the two batches was synthesized at a molten metal bath temperature of 360 °C instead of 350 °C. All batches of particles were purified from the crude reaction mixture by suspending in twice the volume of toluene acting as a solvent, followed by centrifugal precipitation of the nanoparticles using an equal volume of ethanol as an antisolvent. The washing procedure was repeated two to three times before suspending the dried particle pellet in toluene. TEM micrographs were obtained on a Hitachi H7000 100 kV TEM or on a FEI Talos F200i 200 kV S/TEM, by drop casting small volumes of diluted particle solutions in toluene onto 200 mesh Cu/Formvar-carbon or 200 mesh Cu/Carbon grids. Particle physical size distributions were obtained by performing image analysis using ImageJ [82] on at least 500 particles per sample.

2.3. PEG-silane synthesis and ligand exchange

We synthesized the polyethylene glycol-silane conjugate (PEG-silane) used to coat particles via a two-step procedure [83]. First, 5 kDa mPEG was converted to mPEG-acetic acid (mPEG-COOH) using a strong oxidizing agent [84]. Briefly, 50 g of mPEG was dissolved in 400 mL of acetone, and 16.1 mL of Jones Reagent (70 g of chromium trioxide in 500 mL of deionized water and 71 mL of sulfuric acid) was used to oxidize mPEG over 24 h. Approximately 5 mL of isopropyl alcohol was added to stop the reaction and 5 g of activated charcoal was added to remove impurities. The chromium salts and activated charcoal were removed using vacuum filtration. The acetone solution containing the oxidized mPEG was concentrated using a rotary evaporator. The concentrated mixture of mPEG-COOH was re-dissolved in 50 mL of 1 M hydrochloric acid. The polymer was then extracted to the organic phase by liquid − liquid extraction using 150 mL dichloromethane to partition chromium trioxide to the aqueous phase. The mPEG-COOH in dichloromethane solution was concentrated by rotary evaporation. The concentrated mPEG-COOH was precipitated using cold diethyl ether. The mPEG-COOH was then dried in a vacuum oven at room temperature. Proton nuclear magnetic resonance (NMR) spectroscopy was used to confirm full conversion of mPEG to mPEG-COOH. To obtain PEG-silane, an amidation reaction using APTES was performed. APTES was added to melted mPEG-COOH at a 1:1 M ratio at 60 °C, then reacted for 2 h at 120 °C and 500 mbar with constant mixing. The PEG-silane was then collected and cooled to room temperature. The resulting PEG-silane was analyzed through gel permeation chromatography (GPC) to confirm absence of oligomerization.

The nanoparticles were coated with the PEG-silane using ligand exchange, following previously published procedures [85,86]. Briefly, PEG-silane dissolved in dry toluene was mixed with a well-dispersed particle suspension, using a 10x excess of PEG-silane relative to the calculated number of oleic acid chains present on the particle surface. APTES was added at a 5x excess relative to the number of PEG chains and mixed well. The solution was capped and allowed to react overnight, approximately 16 h, at 100 °C. PEG-silane coated nanoparticles were purified using centrifugal precipitation with cold diethyl ether as the antisolvent. This was followed by two cycles of centrifugal precipitation using acetone as the solvent and cold diethyl ether as the antisolvent. The precipitate was then dried in a vacuum oven at room temperature overnight. The following day, PEG-silane coated particles were resuspended in water and dialyzed to remove excess PEG-silane. For further purification, particles were purified using magnetic columns.

Last, the resulting nanoparticles were backfilled with additional mPEG-COOH using EDC-NHS chemistry [81,86]. The number of remaining primary amines on the particles was quantified using CBQCA protein quantification kit, following the manufacturer's protocol. Once the number of amines were determined, a ratio of 1:2 amine: mPEG-COOH was used. The mPEG-COOH was suspended in water and pH adjusted to 5.0. EDC was added at a 1:2 carboxylic acid: EDC ratio and allowed to react for 15 min. Then, sulfo-NHS was added at a 1:1 ratio of EDC: sulfo-NHS. The pH of the solution was slowly adjusted to 7.0 and reacted for 15 min. Last, the nanoparticle solution was added, and the pH adjusted to 9.0. The mixture reacted overnight and was purified using a magnetic column. Finally, the nanoparticle suspension was sterilized using a 0.22 μm PES syringe filter and stored at 4 °C.

2.4. Magnetometry

2.4.1. Nanoparticle sample preparation

Washed and dried nanoparticle samples were prepared using slight modifications for each sample matrix investigated. We refer the reader to Fig. 1 below for a schematic of the general synthesis and sample preparation procedure with a sufficient level of detail for the reader to connect various steps with sections described in our methods. Panel A) in Fig. 1 provides a simple schematic of the nanoparticle synthesis procedure, while panel B) in Fig. 1 outlines the coating and sample preparation strategies we used. Further details on each sample preparation method are provided below.

Particles purified by antisolvent precipitation as described above were redispersed in toluene at concentrations close to ~ 0.1 mg/ml based on dry particle mass, using a combination of water bath sonication and ultrasonication. Dynamic light scattering (DLS) measurements were used to estimate particle hydrodynamic size distribution, and median number-weighted diameter values 5–10 nm larger than the physical diameter of all particle batches were used to confirm absence of agglomeration in the colloidal suspensions. Magnetization measurements were performed on 100 μL of the toluene suspension deposited in polytetrafluoroethylene (PTFE) sample holders manufactured by Quantum Design. In the case of particles coated with PEG-silane, 100 μL of the sterilized nanoparticle solution in water was deposited into the liquid sample holder at ~ 0.1 mg_{Fe}/ml, determined by a colorimetric iron quantification assay [87]. DLS measurements were used to estimate particle hydrodynamic size for the PEG-silane coated particles in water as well, with median number-weighted diameter values 20–30 nm larger than the particle physical size used to confirm successful particle coating as well as absence of agglomeration in the aqueous suspensions.

To prepare powder samples, the thrice washed nanoparticles suspended in toluene were subjected to further particle washing steps, until the particle pellet after centrifugation had lost all traces of waxy organic residue and acquired a matte black grain-textured appearance. The pellet was dried under vacuum for over 24 h, then scraped off the insides of the centrifuge tube and dry-packed into a polycarbonate capsule using a well-cleaned spatula. The powder was tamped down with light tapping and compression to prevent loose movement of the powder within the capsule, and care was taken to leave minimal free space inside. Capsules were held inside clear plastic straws for magnetic measurements, as is common practice with SQuID magnetometers for solid and powder samples.

To disperse particles in docosane and hexatriacontane, 100 μL of toluene suspension was mixed with an equal volume of the melted hydrocarbons and heated at 80 °C for 24 h with regular mixing to help evaporate toluene. A known mass of the waxy dispersion was deposited into the above-mentioned liquid sample holders, and the holders were quenched in cold water after capping, to guard against the possibility of

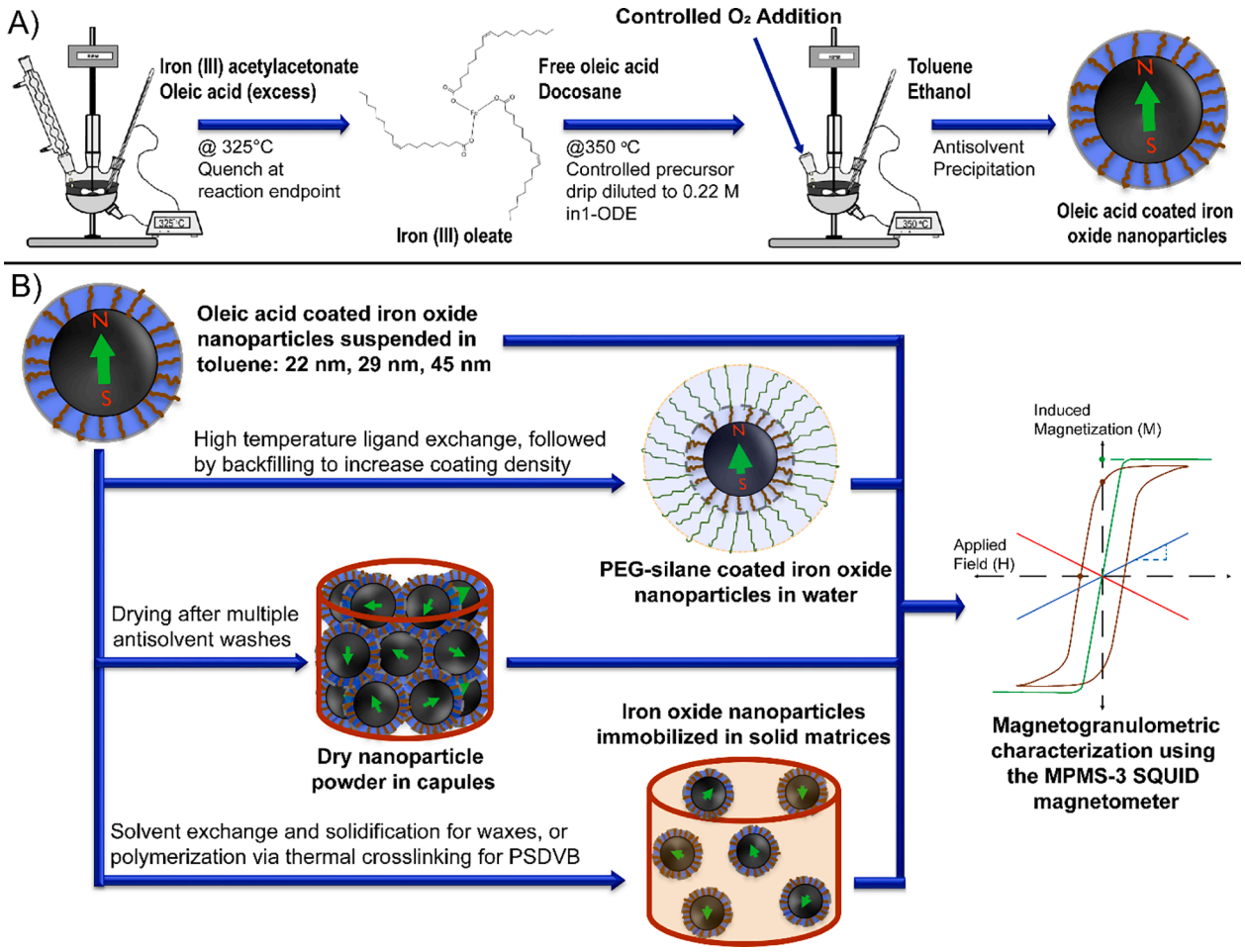

Fig. 1. Schematic for synthesis and sample preparation methods used in this manuscript: A) Semi-batch synthesis methodology used to obtain oleic acid coated iron oxide nanoparticles in the 10–50 nm size range, possessing a tightly controlled physical size distribution and varying crystalline or magnetic properties. We note that the images used are representative, for accurate details of the instrumentation and control parameters used, we refer the reader to our textual descriptions in the relevant methods section. B) Surface modification and sample preparation strategies used with oleic acid coated iron oxide nanoparticles acting as the starting point.

inhomogeneous nanoparticle distribution within the wax due to sedimentation. The filled liquid sample holders were used for magnetic measurements at 300 K, below the melting points of docosane (46 °C or 319 K) and hexatriacontane (76 °C or 349 K).

In the case of hard polystyrene divinylbenzene (PSDVB) matrices, we used methods described previously [73] to make our samples. Briefly, styrene and divinyl benzene monomers were mixed with azobisisobutyronitrile (AIBN) initiator. A known volume of the particle suspensions in toluene were added to this mixture and mixed well in 5 mm ID glass culture tubes. The particle-monomer mixture was heated at 70 °C for 6–8 h to complete the polymerization. Periodic mixing was performed using pipetting in the first hour of polymerization to prevent particle settling, beyond which the crosslinked polymer hardened sufficiently to prevent movement of particles within the matrix. The volumes of particle suspension and PSDVB monomer mix were calculated to ensure that particles remained dilute in the final polymer matrices. The PSDVB samples were held in plastic straws for the magnetic measurements, as is common practice with SQuID magnetometers for solid and powder samples.

2.4.2. Magnetization measurements

Measurements were performed on a Magnetic Property Measurement System-3 (MPMS-3, Quantum Design) superconducting quantum interference device (SQuID) magnetometer. We used a sequence that was validated using a paramagnetic palladium standard sample provided by the instrument manufacturer. To validate instrument operation, we checked that the magnetization data for the Pd sample was linear and free of artifacts over the entire range (±7 T) of measurement for the instrument. Nanoparticle samples were contained either in PTFE liquid sample holders or were placed in plastic straws (in the case of PSDVB and powder samples) and centered at a field of 10 mT.

2.4.3. Magnetogranulometric analysis

Magnetogranulometry was performed on the nanoparticle samples by fitting the measured magnetization data *M(H)* to the Langevin function *L(α)* for superparamagnetism, weighted using a single lognormal magnetic size distribution as suggested by Chantrell et al [24]. In equations (1)-(5) below, ϕ_{mag} is the mass fraction of iron oxide nanoparticles in the sample, M_d is the domain magnetization (446000 A/m [88], value for bulk magnetite), $n_v(D_m)$ is the lognormal distribution function for the magnetic diameter population, α is the Langevin parameter, X_{bkg} is the background susceptibility of the sample, H is the applied magnetic field, μ_0 is the permeability of free space, k_B is Boltzmann's constant and T is the measurement temperature. D_{mv} is the volume weighted median diameter of the magnetic diameter distribution, and ln σ_g is the geometric deviation. The fits were performed in MATLAB 2019b using a non-linear regression model with least-squares fitting.

$$M(H) = \phi_{mag} M_d \int_0^\infty n_v(D_m) L(\alpha) dD_m + X_{bkg} H \quad (1)$$

$$n_v(D_m) = \frac{1}{\sqrt{2\pi}D_m ln\sigma_g} exp[-\frac{ln^2(\frac{D_m}{D_{mv}})}{2ln^2\sigma_g}] \quad (2)$$

$$L(\alpha) = \coth\alpha - \frac{1}{\alpha} \quad (3)$$

$$\alpha = \frac{\pi\mu_0 M_d D_m^3 H}{6k_B T} \quad (4)$$

3. Results and discussion

3.1. Physical size and morphology of particles

The nanoparticles at the end of each synthesis, regardless of use of oxygen during the synthesis, and regardless of the final size, were highly crystalline, faceted and had narrow physical size distributions, as is characteristic of the semi-batch thermal decomposition method used [72,77]. The differences in size and morphology result from the varying conditions used for each synthesis, described in the methods section of this manuscript. The nanoparticle batch named "22A" in Fig. 2 has a number-weighted median diameter (D_p) of 22.5 nm and a ln σ_g of 0.11. Batch "22B" had D_p = 20.5 nm and ln σ_g = 0.11. Batch "29A" had D_p = 29.5 nm and ln σ_g = 0.09, while batch "29B" has D_p = 29.3 nm and ln σ_g = 0.08. Lastly, the "45 nm" particles are 44.8 nm in number-weighted median diameter with a ln σ_g of 0.09. Batches 22A, 29A and 45 nm were used for the measurements made in toluene, docosane, hexatriacontane, and PSDVB. The 45 nm particles were used for the powder measurement. Batches 22B and 29B were synthesized to evaluate the influence of measurement temperature and surface coating thickness on the measured magnetization data for nanoparticle suspensions, and on the magnetic diameter distributions obtained from corresponding magnetogranulometric fits.

3.2. Validating the measurement sequence using a palladium sample

Removal of remanent magnetization in the sample as well as residual flux in the magnetometer coils has been found to be critical for obtaining measurements that are representative of the real behavior of a magnetic sample. This is typically achieved by using a degaussing sequence [89]. The MPMS-3 SQuID magnetometer used to perform magnetic measurements has a built- in function that performs the degaussing, namely the 'Magnet Reset' command, but inadvertent omission of the degaussing step can lead to measurements with systematic and persistent error over the entire range of applied magnetic field values probed. We tried three different variants of the degaussing protocol in our MPMS- 3 SQuID magnetometer. Results are presented in Fig. 3. As seen, a measurement sequence with no degaussing protocol (Fig. 3A) results in a magnetization curve with artificial hysteresis. Adding a manually constructed oscillatory degaussing protocol (Fig. 3B) when moving from high field to low field (at a selected crossover value of 100 mT) partially removes the artifact but does not eliminate it. We concluded that a sequence with magnet reset steps performed after sample centering, and whenever the field value goes from high field to low field (at a crossover value of 100 mT) worked best to remove this hysteresis artifact and obtain the expected paramagnetic behavior for the Palladium sample (Fig. 3C). This sequence was used for all subsequent nanoparticle magnetization measurements.

To help readers better interpret the figures in our work, we will use Fig. 3 as a reference to provide detailed notes and use the same notation for all magnetization data presented hereafter. We use different markers to differentiate between data points on figures as follows: open circles represent a ± 2 mT "low field magnetization loop" obtained at intervals of 0.1 mT (or 1 Oe) after the sample was centered and a magnet reset was performed. To obtain closed loop data over the full measurement range, field was varied from 0 mT to 2 mT, down to −2 mT, and up to 2 mT. Next, the field is ramped up to + 7 T at appropriate field spacing

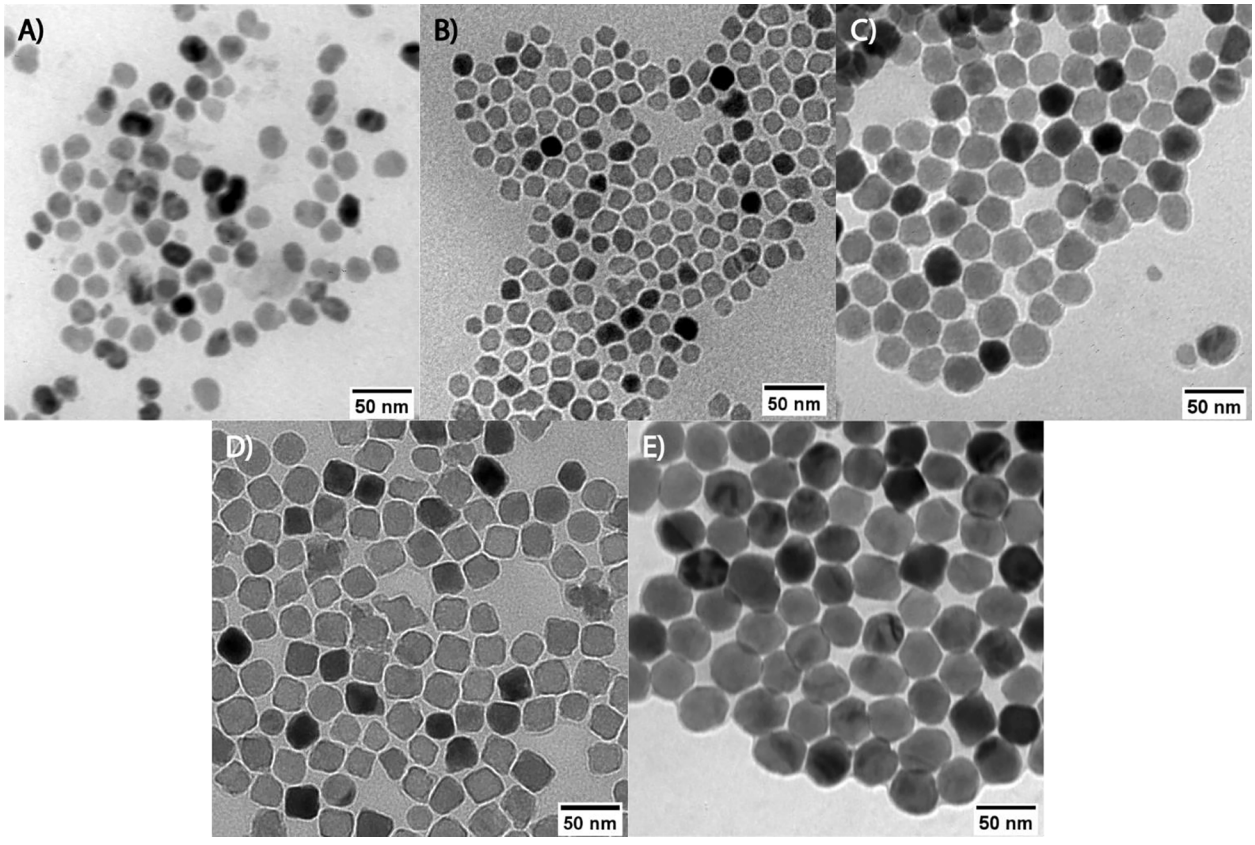

Fig. 2. TEM micrographs of selected particle batches: A) 22A, B) 22B, C) 29A, D) 29B and E) 45 nm.

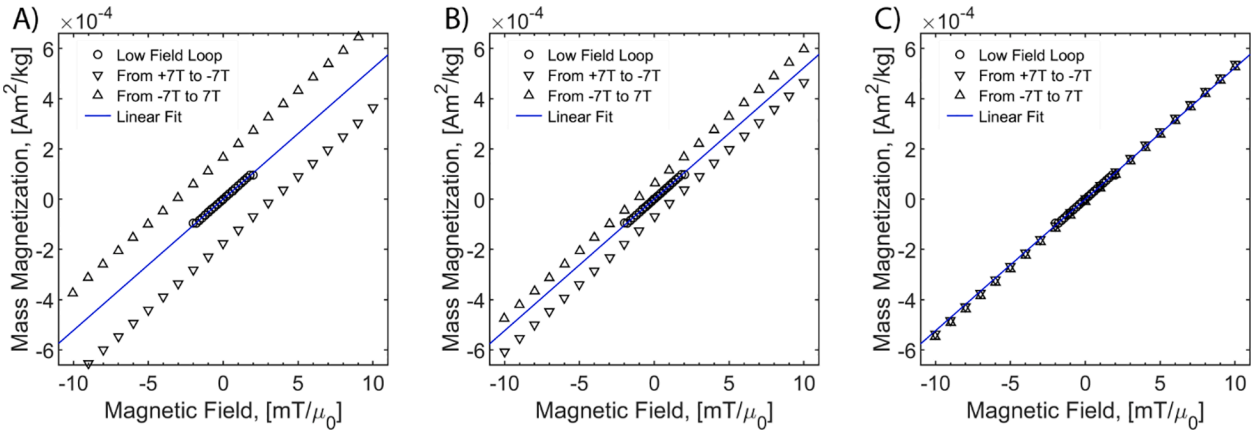

Fig. 3. Low field magnetization data of Pd sample at 300 K with A) No degaussing protocol, B) using an oscillatory degaussing sequence at a crossover value of ± 100 mT and C) Magnet reset at a crossover value of ± 100 mT. For better visualization, we plot only low field data between ± 10 mT, but all measurements were obtained over a range of ± 7 T. The solid (blue) lines correspond to the expected paramagnetic magnetization response of the Pd sample, shown to highlight deviations from paramagnetic behavior where it is present.

(data not shown in all figures), and ramped down using the same field intervals to −7 T. Downward facing triangles in our figures represent the segment of data between ± 10 mT obtained going "down" from + 7 T to −7 T. To close our magnetization loop, the same field spacing was then used to go from −7 T to + 7 T. Upward facing triangles in our figures represent the data between ± 10 mT obtained going "up" from −7 T to 7 T. As noted earlier, magnet resets were performed when the field reached ± 100 mT, in the direction of decreasing field magnitude.

3.3. Measurements of nanoparticles as dry powders

In (Fig. 4A), the nanoparticles are immobilized in a microporous chemically crosslinked hard polymer matrix PSDVB [73,78,79], and this eliminates all particle motion. Additionally, the particles are well dispersed and dilute within the matrix, resulting in a ferromagnetic magnetization response with a symmetric hysteresis loop. The coercive field measured while going from + 7 T to −7 T is comparable to the coercive field measured moving in the opposite direction, and the susceptibility (slope of the magnetization data) measured for the "low field", "down" and "up" parts of the loop are constant over the range of data displayed. On the other hand, when measured in powder form (Fig. 4B) it is observed that the particles attain zero moment and align with the reversed direction of the field at a much smaller value of magnetic field. In addition, the magnetization curve is not symmetric about zero field, and the susceptibility changes drastically at low field values to achieve this response. We attribute this apparent enhanced susceptibility and the artificially reduced coercivity to a mechanism where the loosely packed particles physically move (rotate or translate) to align with the magnetic field. The asymmetry in the magnetization data can be explained by considering that the powder was packed in one arrangement when the measurement was started. Thus, in the "down from + 7 T to −7 T" part of the loop, this ordered packing of particles undergoes rearrangement to align with the reversed field. On the way "up from −7 T to + 7 T", the powder experiences the same field values and field ramp rates, except with a different local packing order. Thus, the rearrangement that occurs to align with the field direction is similar, but not identical to the changes experienced in the "down" loop. Regardless of the mechanism, the measurements shown in Fig. 4 demonstrate that artifacts are significant in powder measurements for large particles.

3.4. Measurements in liquid solvents

Measurements with the nanoparticles suspended in a liquid are a way of obtaining data for magnetogranulometric fitting due to the concept of extrinsic superparamagnetism [75,76] mentioned above. The data

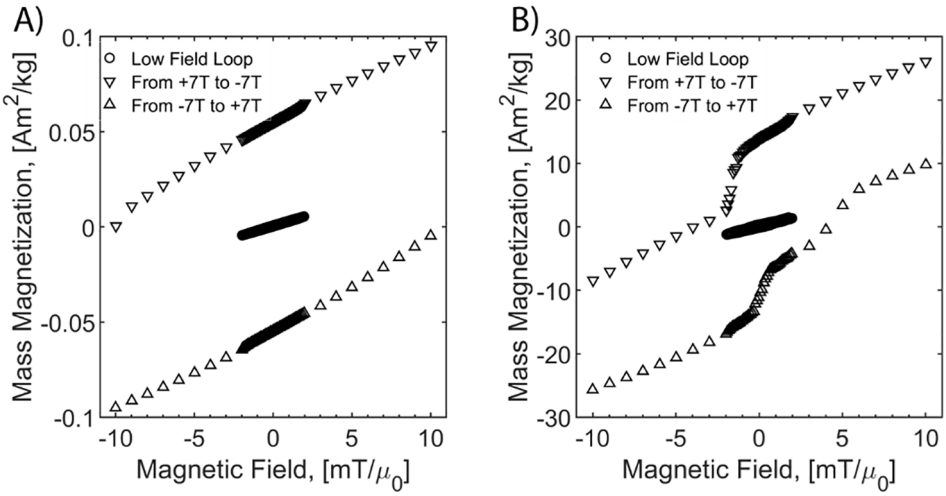

Fig. 4. Low field magnetization data for 45 nm particles A) immobilized in a hard PSDVB matrix to eliminate all particle motion B) as a dry powder loose packed in a gel capsule. For better visualization, we plot only low field data between ± 10 mT, but all measurements were obtained over a range of ± 7 T.

presented in Fig. 5 shows that magnetogranulometry using the Langevin function weighted with a lognormal magnetic size distribution fails to capture the non-Langevin behavior that appears at low fields for all particle sizes tested, making the assignment of physical significance to predictions of particle properties arising from the fits inaccurate. We observe that deviations from Langevin behavior can be identified as an opening of the hysteresis loop at low fields, and abrupt changes in the measured susceptibility close to zero field. This is similar to the non-Langevin behavior seen at low fields in powder samples. Additionally, the degree of deviation increases as particle size increases. One possible explanation is that the strength of interparticle dipole–dipole interactions in a small non-zero external field increases as the size of nanoparticles increases. In a liquid, particles can move towards each other, forming chains and aggregates due to dipole–dipole interactions [46,90]. These chains and aggregates will not respond to an applied field the same way isolated non-interacting particles would, which is a basic assumption of the Langevin function. Hence, we hypothesize that the deviations from Langevin behavior appearing in Fig. 5 are evidence of the formation of chains of nanoparticles as the sample is magnetized in the direction of the applied DC field, and a reversal of the chain polarity each time the field direction is reversed.

Similar artifacts were observed with another batch of particles (29B) possessing similar physical and magnetic properties as 29A when measurements were performed in toluene (Fig. 6A). In Fig. 6B, we measured the magnetization response of 29B particles coated with a thick (5 kDa) polyethylene glycol brush and found that the particle magnetization response conforms to Langevin behavior. This suggests that particle interaction artifacts in magnetization measurements for large nanoparticles can be prevented by using appropriate surface coating strategies, such as the dense polyethylene glycol brush used here [86], which offers steric stabilization to the particles by physically increasing the minimum separation distance. Indeed, several other groups have performed work that demonstrates formation of nanoparticle chains in nanoparticle suspensions under the action of static magnetic fields [90–99], in several of the articles the thickness and grafting density of the attached ligands was found to influence the degree of chaining. However, none of the work cited above examines the influence of the coating thickness on equilibrium magnetization measurements as shown here.

We note here that observations reported in Fig. 6 are specific: a dense 5 kDa PEG-silane coating, with a brush thickness of approximately 10–15 nm based on DLS measurements, was found sufficient to eliminate particle–particle interactions and result in Langevin behavior during magnetization measurements for the 29 nm iron oxide nanoparticles. However, particles with varying core sizes would, in theory, need different coating thicknesses to achieve extrinsic superparamagnetism [75,76] and display Langevin behavior. In general, larger particles would require thicker coatings, because the magnitude of attractive magnetic dipolar interactions between particles increases as a function of particle volume. To obtain a precise estimate of coating thickness required, one must consider the balance between several competing forces that influence the stability of colloidal suspensions of magnetic nanoparticles, such as: magnetic particle–particle dipolar forces (attractive), Van der Waals forces (attractive), electrostatic forces (repulsive), hydrogen bonding and the hydrophobic effect (attractive), osmotic pressure (typically attractive), non-charge transfer Lewis acid-Lewis base interactions (attractive), steric interactions (typically repulsive) and thermal motion (attractive or repulsive). These force balances can be accounted for using the DLVO theory [100–102] for interactions in colloidal suspensions, or with other theories [103] that have been developed to account for non-DLVO interactions present in many suspensions.

3.5. Measurements in wax and polymer matrices

In Fig. 7, we investigate the influence of another sample preparation method by embedding the particles in hydrocarbon waxes that have melting points high enough to be solid at room temperature. Unlike Figs. 3-6, we do not present the “down” and “up” segments of data in Fig. 7. Instead, we assess the “low field loop” between ± 2 mT for its adherence to Langevin behavior in docosane (open circles), hexatriacontane (open squares) and PSDVB (upward pointing triangles). (Fig. 7A) demonstrates that the 22 nm (22A) particles show the defining characteristics of Langevin behavior in the low field linear regime for all solid sample matrices tested, namely: no hysteresis or a “closed loop” magnetization response, and a single value of initial susceptibility (defined as the slope of the magnetization vs. external field data in the linear regime). Differences in the susceptibility of individual measurements arise from small differences in the mass fraction of particles in the solid matrices. Similar behavior is seen for 29A and 45 nm particles in PSDVB matrices (upward triangles, Fig. 7B and 7C), with a smoothly varying magnetization response and a single value of initial susceptibility. We make a note that the response for 29A particles in PSDVB is not strictly “linear” or “closed loop”, which could be due to the large thermally blocked ferromagnetic nanoparticles retaining magnetization from previous exposure to a large external field value. However, remanent magnetization alone cannot explain the artifacts seen for 29A and 45 nm particles in docosane (open circles, Fig. 7B and 7C) and hexatriacontane (open squares, Fig. 7B and 7C)- the collective magnetization of nanoparticles retains a linearly decreasing non-zero value

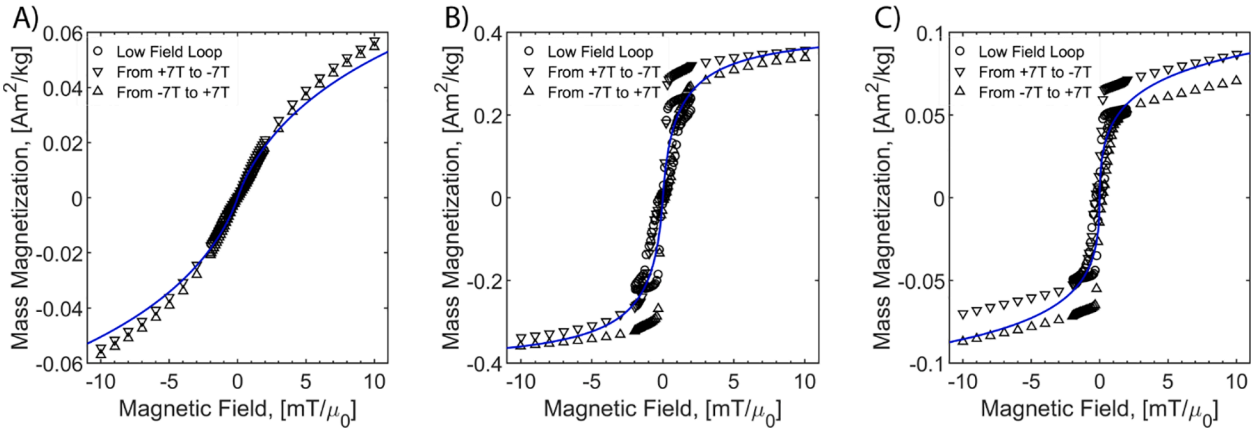

Fig. 5. Measurements at 300 K in toluene for A) 22A particles B) 29A particles C) 45 nm particles coated in oleic acid. For better visualization, we plot only low field data between ± 10 mT, but all measurements were obtained over a range of ± 7 T. Solid (blue) lines correspond to the expected Langevin response based on magnetogranulometric fits to the Langevin function weighted with a lognormal magnetic diameter distribution, shown to highlight deviation from ideal Langevin behavior where it is present.

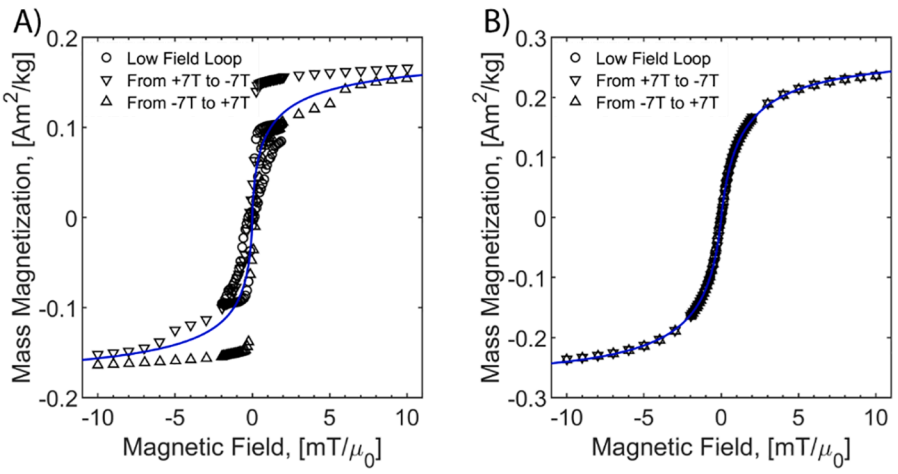

Fig. 6. Measurements for 29B particles at 300 K, A) coated in oleic acid and suspended in toluene B) coated in a dense thick brush of polyethylene glycol suspended in water. For better visualization, we plot only low field data between ± 10 mT, but all measurements were obtained over a range of ± 7 T. Solid (blue) lines correspond to the expected Langevin response based on magnetogranulometric fits to the Langevin function weighted with a lognormal magnetic diameter distribution, shown to highlight deviation from ideal Langevin behavior where it is present.

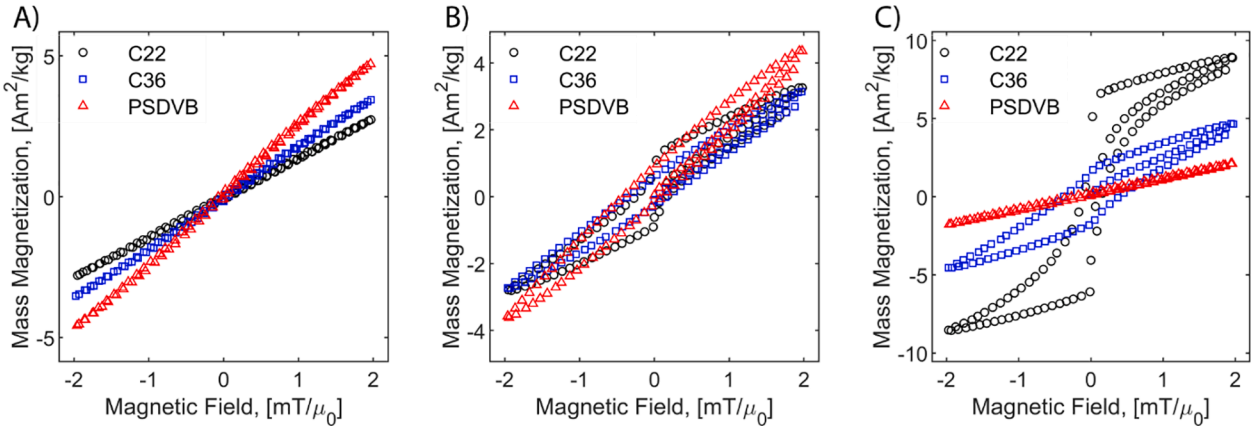

Fig. 7. Low field magnetization loops for A) 22A, B) 29A, and C) 45 nm particles in hydrocarbon wax and PSDVB matrices at 300 K. For better visualization, we plot only the "low field loop" between ± 2 mT, but all measurements were obtained over a range of ± 7 T. Different markers in each panel are used to denote measurements performed in different solid sample matrices.

until the external applied field is below 0.1 mT, following which the measured magnetization rapidly decreases to a new value that aligns with the external field when it changes direction. This "flip switch" response bears features that are like the response seen for oleic acid coated nanoparticles suspended in toluene (Figs. 5 and 6A), and so we present parallel reasoning to explain it.

First, we remind the reader that PSDVB formed by thermal crosslinking is typically a hyper-crosslinked polymer [78,79] with predominantly microporous structure (average pore size smaller than 5 nm). Previously, our lab has used PSDVB to successfully immobilize particles with D_p ranging from 8.5 nm to 11 nm for magnetogranulometric measurements [62]. Thus, the hard PSDVB matrix was found to restrict particle physical motion completely, resulting in smoothly changing low field magnetization loops even for the larger particles. On the other hand, docosane and hexatriacontane are solidified waxy alkanes with no chemical crosslinking. As such, they have a mechanical stiffness much higher than liquid solvents such as toluene but are significantly softer than a hard polymer matrix such as PSDVB. Additionally, N-alkanes have been studied previously for the presence of pre-melting phase transitions that lead to an increase in the conformational disorder, longitudinal translation ability and interchain distances within unit cells at temperatures between 10 and 40 K below their macroscopic melting point [104,105]. For our measurements performed at 300 K, a higher degree of deviation from Langevin behavior was observed in docosane (with a macroscopic melting point of 319 K) than in hexatriacontane (with a macroscopic melting point of 349 K) for both 29A and 45 nm particle batches. The differences in the ability of these two solid matrices to suppress inter-particle interactions would then be well-explained if we acknowledge that the waxes at 300 K may have interchain distances that allow limited movement of particles with dimensions comparable to the chain length of the alkanes. Contrary to the case in liquid solvents, where large particles translate within the suspension and form chains of particles magnetized in the same direction, we propose that waxy alkanes restrict particle physical translation but allow rotational polarization leading to the "flip switch" changes in the measured magnetization. Building upon our hypothesis of physical particle motion causing the appearance of artifacts in magnetization data, we propose that the behavior observed in Fig. 7 for large particles is caused by a combination of slow randomization of particle dipole orientations while the external static field is decreasing in a stepwise fashion, followed by rapid (and collective) particle physical rotation with an enhanced apparent susceptibility to align with the external field when it changes direction.

3.6. *Measurements in PSDVB as a function of temperature and analysis of magnetogranulometric fitting results for selected samples*

To conclude, we discuss the influence of measurement temperature, and selected sample preparation methods on the particle magnetic diameter distributions obtained by applying magnetogranulometric fits using the Langevin function weighted with a lognormal magnetic size distribution. First, we obtained ZFC/FC measurements on both particle

batches used here to estimate their blocking temperatures (T_b). Batches 22B and 29B have $T_b = 127$ K and $T_b > 400$ K (outside the temperature range of our instrument). respectively. We make a note that the simple parabolic fit we used to determine the peak in the ZFC curves may be overestimating the blocking temperature of the nanoparticles according to recent work exploring the effect of interparticle interactions on ZFC/FC data [44] but justify the simplistic model because we use the value only for qualitative comparisons between measurement temperature and blocking temperature. In Fig. 8, we present the magnetization response of nanoparticles (22B) immobilized in a PSDVB matrix as a function of measurement temperature. As seen in (Fig. 8A), the magnetization response for 22B at 100 K exhibits hysteresis, which is expected for superparamagnetic particles below the blocking temperature. (Fig. 8B), obtained at 200 K, is above the blocking temperature of the particles, which coincides with closing of the hysteresis loop, although there is still significant deviation from Langevin behavior. (Fig. 8C and 8D), at 300 K and 400 K, are far above the blocking temperature, which is why they exhibit closed loop magnetization responses as well, and the response is closer to the expected Langevin behavior.

Finally, we conduct a closer examination of the results obtained from the magnetogranulometric fits for selected samples. To assess whether we should assign physical significance to the magnetic diameter distributions obtained from a given fit, our primary criterion was simply whether the predicted magnetic size estimate is smaller than the physical size of the particles. This is because iron oxide nanoparticles synthesized by the thermal decomposition method are known to typically possess a magnetically dead layer [23,72] or non-magnetic phases of iron oxide such as wüstite [70,71], which lead to a reduction in the magnetic size. Our second criterion was the adherence of the fitted function to the measured data. Aside from confirming whether the fit prediction had a close match across the entire range of magnetization data by plotting both the full range and low field data separately, we used the absolute root mean squared error (RMSE) of the non-linear regression as one of the parameters to differentiate between fits performed for the same particle sample. In addition, the non-linear regression allowed us to obtain 95% confidence intervals for each fitting parameter. In some cases, these confidence intervals were used along with the predictions to make decisions regarding the validity of the magnetogranulometric analysis. To aid discussion, the values for nanoparticle mass fraction in the sample (ϕ_{mag}), volume-weighted median magnetic diameter (D_{mv}), corresponding geometric deviation (ln σ_g), background susceptibility at high field (X_i), 95% confidence intervals for each of the four fit parameters, and the RMSE of the fit are listed for 22B particles as a function of temperature (first 4 entries), and 29B particles with different surface coating thickness and medium of suspension (entries 5–7) in Table 1.

For entries in Table 1 corresponding to data for the 22B particles in a solid matrix (Fig. 8), we see that the magnetic diameter estimate increases as the measurement temperature increases past the blocking temperature of the particles (127 K for batch 22B). This can be explained by the increasingly larger fraction of the nanoparticles that become thermally unblocked when the measurement temperature increases, and the expectation that larger particles require higher temperatures to become unblocked. When compared to the physical size distribution of the particles ($D_p = 20.5$ nm and ln $\sigma_g = 0.09$), the magnetic diameter estimate approaches the physical diameter. Looking further, the 95% confidence intervals for all the estimates become narrower as temperature increases from 100 K to 300 K, and the RMSE of the fit drops as

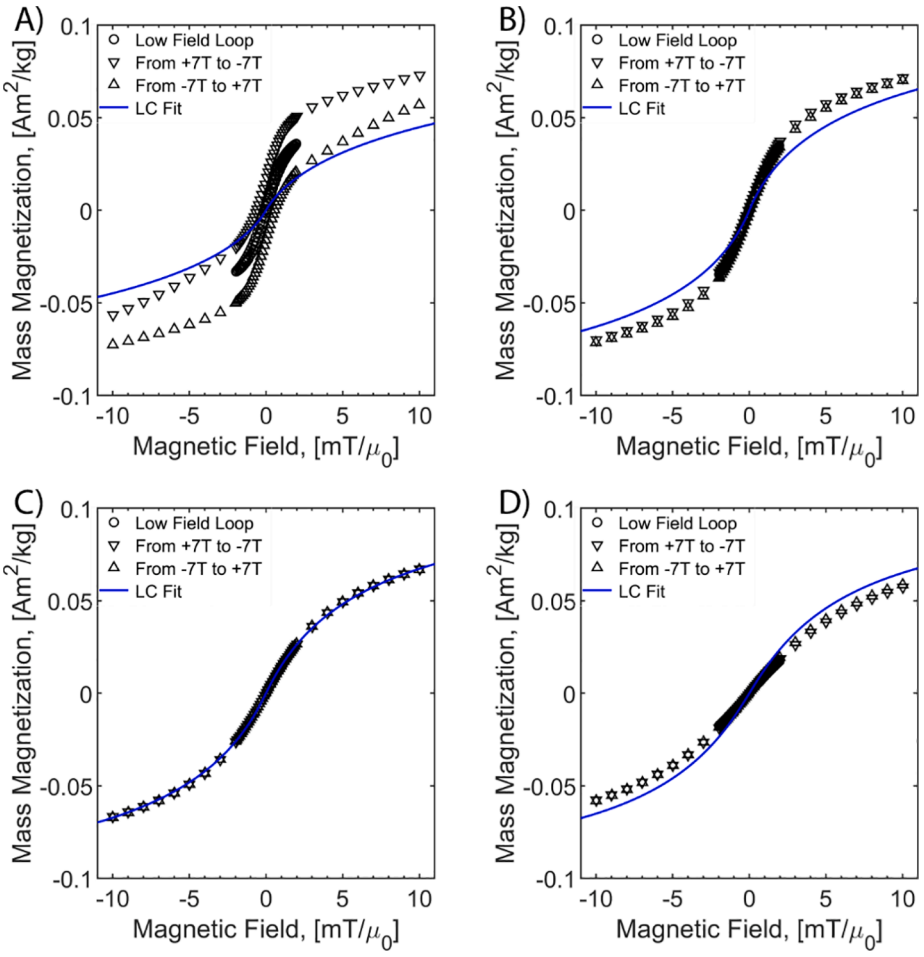

Fig. 8. Low Field magnetization loops for 22B particles in PSDVB at A) 100 K, B) 200 K, C) 300 K, and D) 400 K. For better visualization, we plot only low field data between ± 10 mT, but all measurements were obtained over a range of ± 7 T. Solid (blue) lines correspond to expected Langevin response based on magnetogranulometric fits to the Langevin function weighted with a lognormal magnetic diameter distribution, and are shown both to aid discussion, and to highlight deviation from ideal Langevin behavior where it is present.

Table 1
Magnetic diameters obtained from data obtained using different sample preparation methods.

Particle Batch, Media, Temperature	Magnetic Diameter distributions obtained from magnetogranulometric analysis using the Langevin function. Numbers in parentheses represent 95% confidence intervals for the fit predictions obtained via non-linear regression analysis in MATLAB.				
	ϕ_{mag} (*10^{-2}, a.u.)	D_{mv} (nm)	ln σ_g (a.u.)	X_i (*10^{-10}, a.u.)	RMSE (a.u.)
22B, PSDVB, 100 K	0.151 (±0.005)	10.91 (±0.52)	0.582 (±0.059)	−10 (±13)	0.00874
22B, PSDVB, 200 K	0.145 (±0.001)	14.79 (±0.08)	0.462 (±0.008)	−1.2 (±1.7)	0.00128
22B, PSDVB, 300 K	0.135 (±0.000)	16.32 (±0.05)	0.356 (±0.005)	0.0 (±0.9)	0.00061
22B, PSDVB, 400 K	0.121 (±0.000)	17.14 (±0.07)	0.268 (±0.007)	0.0 (±1.1)	0.00083
29B, Oleic acid coated in toluene, 300 K	0.220 (±0.009)	31.50 (±2.0)	0.662 (±0.146)	0.0 (±33)	0.02648
29B, PSDVB, 300 K	0.037 (±0.000)	11.07 (±0.16)	0.050 (±0.114)	0.0 (±1.5)	0.00101
29B, PEG coated in water, 300 K	0.328 (±0.002)	28.00 (±0.19)	0.416 (±0.017)	0.0 (±6.8)	0.00464

well. Going from 300 K to 400 K, confidence intervals of some parameters in the fit increase, and the RMSE of the fit increases as well. These observations are also reflected in the closer match of the magnetogranulometric fit at 300 K across the entire range of measured magnetization data, which is not the case for the fits obtained at other temperatures, as depicted in Fig. 8 for the low field region of the data.

Next, we look at entries 5–7 of Table 1 to examine the influence of surface coating and medium of suspension on the magnetogranulometric predictions. We remind readers that the 29B particles had a $T_b > 400$ K, thus they are ferromagnetic over the entire range of temperatures our instrument can access. To aid discussion, in Fig. 9 we plot the magnetization data corresponding to those table entries across selected ranges of applied external field to visualize the non-Langevin behavior present in the samples. When coated with oleic acid and suspended in toluene (Fig. 9A,9B and 9C), the first indicator that particle motion artifacts make magnetogranulometric fits unreliable is that the predicted magnetic size is larger than the physical size ($D_p = 29.3$ nm and $\ln \sigma_g = 0.09$) of the nanoparticles. The second obvious issue with the fit is that it does not provide a close match to the measured magnetization data, this can be easily confirmed by looking at the low field (±10 mT) and mid-range (±100 mT) plots of the fit and magnetization data. However, it is difficult to see the deviations from Langevin behavior in the full range data. We wish to emphasize that most authors (including our group in the past) typically plot only the full range data, and this makes it incredibly easy for the deviations to be obscured. Next, the sample in PSDVB (where the 29B particles are immobilized and thermally blocked, data in Fig. 9D, 9E, and 9F) resulted in a magnetic diameter estimate well below the physical size of the particles, and the 95% confidence intervals seem reasonable in comparison to fit predictions, but the inability of the fit to provide a close match to the ferromagnetic magnetization response is again verified by looking at low field and mid-range plots of the data. Thus, we designate the fit as unreliable. Finally, the 29B particles present Langevin behavior when coated with a sufficiently thick surface coating (Fig. 9G, 9H and 9I). Consequently, the magnetogranulometric fit provides a close match to the measured magnetization response at both low and high field ranges, which is reflected in the low RMSE value for the fit. To further cement our confidence in the magnetic diameter estimate obtained from the fit, we observe that the confidence intervals for all fit parameters are narrow, and that the predicted magnetic size matches the physical size distribution, which has been demonstrated previously for particles synthesized with methods that promote better phase selectivity in the synthesized particles by providing an oxidizing environment through varied mechanisms [68,71,72]. This observation lends credibility to the idea that large thermally blocked particles may be analyzed reliably for their magnetic size in liquid suspensions, by taking advantage of the extrinsic superparamagnetism [75,76] endowed when sufficiently thick surface coatings that impart steric stabilization are employed. As a final note in this discussion, we point out that making comparisons of the width of confidence intervals and the absolute value of the RMSE across 29B samples cannot provide further insight, because three separate samples (with different mass fractions, suspension media, and surface coating of the nanoparticles) were used to obtain these measurements. Comparison across the 4 measurements for 22B particles was possible only because the same sample was measured at different temperatures.

4. Conclusions

Equilibrium magnetization measurements of magnetic nanoparticles can be confounded by several particle motion artifacts arising from sample preparation that affect the interpretation and ability to use the data for more detailed analysis, especially for large magnetic nanoparticles. In this work, we show that measurements in liquid solvents can be affected by particle–particle interactions that may result in the formation of nanoparticle chains, resulting in non-Langevin behavior at low fields, even though the particles are able to freely rotate and align with the applied field. The effect was demonstrated to become significant with increasing particle physical size, which can be attributed to the increasing strength of dipolar interactions between larger particles. Magnetogranulometric fits using the Langevin function could not capture particle magnetic response in these cases. Further, we demonstrated that these artifacts can be suppressed to yield Langevin behavior in the magnetization curves when the nanoparticles are sterically stabilized by the addition of a sufficiently thick brush-like surface coating, which can be explained by the fact that dipolar interactions would become increasingly insignificant when interparticle separation is increased. Magnetogranulometric fits on the sterically stabilized magnetic nanoparticles in aqueous suspension resulted in magnetic size distributions that show agreement with the physical size distribution of the particles, even for large thermally blocked particles. Next, we demonstrated that use of waxy solids, such as long-chain hydrocarbons, can result in non-Langevin behavior for large particle sizes, and this is attributed to a rotational polarization effect where the particle magnetic dipoles align with the field and retain their orientation until the externally applied field reverses direction. This is fundamentally different from the way particles behave in liquid because the particles are no longer free to translate, but particle rotation is hindered only partially. Lastly, we show that to obtain data free of particle motion artifacts, measurements need to be performed in a rigid solid matrix, such as the polymer matrix PSDVB. For measurements performed with particles immobilized in such a fashion, magnetic diameter distributions obtained from a Langevin fit are influenced by measurement temperature. Measurements below the blocking temperature of the particles display hysteresis, as expected of single domain magnetic nanoparticles in the thermally blocked regime. As the measurement temperature increases, magnetic diameter estimates increase, which is consistent with the expectation that more of the large particles in the sample become thermally unblocked.

CRediT authorship contribution statement

Shehaab Savliwala: Conceptualization, Methodology, Software, Validation, Formal analysis, Investigation, Writing – original draft, Writing – review & editing. **Sitong Liu(刘思彤):** Methodology, Validation, Investigation, Writing – review & editing. **Carlos M. Rinaldi-Ramos:** Conceptualization, Software, Resources, Writing – review & editing, Supervision, Funding acquisition.

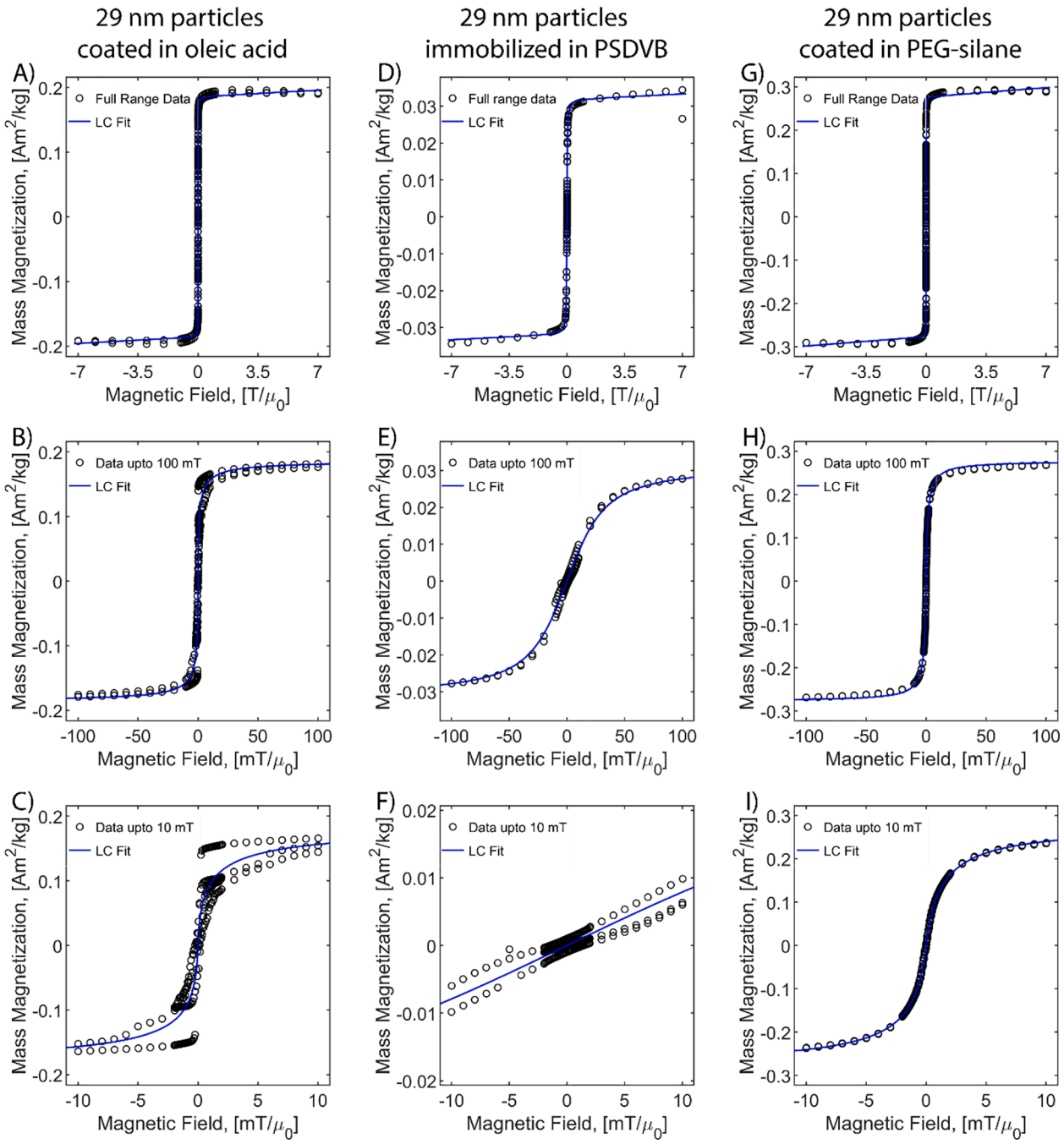

Fig. 9. Magnetization data for 29B particles taken with the particles coated in oleic acid and suspended in toluene between A) ± 7 T B) ± 100 mT C) ± 10 mT, for 29B particles embedded in a hard PSDVB matrix between D) ± 7 T E) ± 100 mT F) ± 10 mT, and for 29B particles suspended in water with a thick PEG coating for steric stabilization between G) ± 7 T H) ± 100 mT I) ± 10 mT. Solid (blue) lines correspond to expected Langevin response based on magnetogranulometric fits to the Langevin function weighted with a lognormal magnetic diameter distribution, and are shown both to aid discussion, and to highlight deviation from ideal Langevin behavior where it is present.

Declaration of Competing Interest

The authors declare that they have no known competing financial interests or personal relationships that could have appeared to influence the work reported in this paper.

Acknowledgements

We thank Dr. Kyle Allen (UF BME) for insightful discussion regarding our interpretations of the magnetogranulometric fitting data shown here.

Funding Sources

This work was supported by the National Science Foundation [Grant #1727930].

References

[1] A. Einstein, Über die von der molekularkinetischen Theorie der Wärme geforderte Bewegung von in ruhenden Flüssigkeiten suspendierten Teilchen, Ann. Phys. 322 (8) (1905) 549–560.

[2] P. Langevin, "The theory of brownian movement," (in French), *Comptes Rendus Hebdomadaires Des Seances De L Academie Des Sciences,* Letter 146 (1908) 530–533.

[3] D. S. Lemons and A. Gythiel, "Paul Langevin's 1908 paper "On the Theory of Brownian Motion" ["Sur la théorie du mouvement brownien," C. R. Acad. Sci. (Paris) 146, 530–533 (1908)]," *American Journal of Physics,* vol. 65, no. 11, pp. 1079-1081, 1997/11/01 1997, doi: 10.1119/1.18725.

[4] M. von Smoluchowski, Zur kinetischen Theorie der Brownschen Molekularbewegung und der Suspensionen, Ann. Phys. 326 (14) (1906) 756–780.

[5] C. Kittel, Theory of the Structure of Ferromagnetic Domains in Films and Small Particles, Phys. Rev. 70 (11-12) (1946) 965–971.

[6] L. Neel, "Theorie du trainage magnetique des ferromagnetiques en grains fins avec applications aux terres cuites," *Ann. Geophys.,* vol. 5, pp. 99-136, 1949 1949.

[7] E.C. Stoner, E.P. Wohlfarth, "A MECHANISM OF MAGNETIC HYSTERESIS IN HETEROGENEOUS ALLOYS," (in English), *Philosophical Transactions of the Royal Society of London Series a-Mathematical and Physical Sciences,* Article 240 (826) (1948) 599–642, https://doi.org/10.1098/rsta.1948.0007.

[8] W.F. Brown, "Ferromagnetic domains and the magnetization curve," (in English), *J. Appl. Phys.* Article 11 (3) (1940) 160–172, https://doi.org/10.1063/1.1712753.

[9] W.F. Brown, "FUNDAMENTAL THEOREM OF THEORY OF FINE FERROMAGNETIC PARTICLES," (in English), *Ann. N. Y. Acad. Sci.* Article 147 (A12) (1969) 463, https://doi.org/10.1111/j.1749-6632.1969.tb41269.x.

[10] A.D. Fokker, Die mittlere Energie rotierender elektrischer Dipole im Strahlungsfeld, Ann. Phys. 348 (5) (1914) 810–820.

[11] A. Kolmogoroff, Über die analytischen Methoden in der Wahrscheinlichkeitsrechnung, Math. Ann. 104 (1) (1931/12/01 1931,) 415–458, https://doi.org/10.1007/BF01457949.

[12] Collected Papers of L.D. Landau, Elsevier, 1965, pp. 101–114, https://doi.org/10.1016/B978-0-08-010586-4.50023-7.

[13] T.L. Gilbert, A phenomenological theory of damping in ferromagnetic materials, IEEE Trans. Magn. 40 (6) (2004) 3443–3449, https://doi.org/10.1109/TMAG.2004.836740.

[14] H. Vogel, "The temperature dependence law of the viscosity of fluids," (in German), *Physikalische Zeitschrift,* Article 22 (1921) 645–646.

[15] G.S. Fulcher, ANALYSIS OF RECENT MEASUREMENTS OF THE VISCOSITY OF GLASSES, J American Ceramic Society 8 (6) (1925) 339–355.

[16] W.M. Saslow, SCENARIO FOR THE VOGEL-FULCHER LAW, Physical Review B 37 (1) (Jan 1988) 676–678, https://doi.org/10.1103/PhysRevB.37.676.

[17] N. Akulov, Über die Magnetostriktion der Eiseneinkristalle, Zeitschrift für Physik 52 (5) (1929/05/01 1929,) 389–405, https://doi.org/10.1007/BF01339430.

[18] N.S. Akulov, Zur Theorie der Magnetisierungskurve von Einkristallen, Zeitschrift für Physik 67 (11) (1931/11/01 1931,) 794–807, https://doi.org/10.1007/BF01390760.

[19] C.P. Bean, I.S. Jacobs, "MAGNETIZATION OF A DILUTE SUSPENSION OF A MULTIDOMAIN FERROMAGNETIC," (in English), *J. Appl. Phys.* Article 31 (7) (1960) 1228–1230, https://doi.org/10.1063/1.1735809.

[20] C.P. Bean, J.D. Livingston, Superparamagnetism, J. Appl. Phys. 30 (4) (1959/04/01 1959,) S120–S129, https://doi.org/10.1063/1.2185850.

[21] C.E. Johnson, W.F. Brown, Stoner-Wohlfarth Calculation on Particle with Both Magnetocrystalline and Shape Anisotropy, J. Appl. Phys. 30 (4) (1959) S320–S322, https://doi.org/10.1063/1.2185955.

[22] A.E. Berkowitz, W.J. Schuele, P.J. Flanders, Influence of Crystallite Size on the Magnetic Properties of Acicular γ-Fe2O3 Particles, J. Appl. Phys. 39 (2) (1968/02/01 1968,) 1261–1263, https://doi.org/10.1063/1.1656256.

[23] R. Kaiser, G. Miskolczy, Magnetic Properties of Stable Dispersions of Subdomain Magnetite Particles, J. Appl. Phys. 41 (3) (1970/03/01 1970,) 1064–1072, https://doi.org/10.1063/1.1658812.

[24] R.W. Chantrell, J. Popplewell, S.W. Charles, "MEASUREMENTS OF PARTICLE-SIZE DISTRIBUTION PARAMETERS IN FERROFLUIDS," (in English), *Ieee Transactions on Magnetics,* Article 14 (5) (1978) 975–977, https://doi.org/10.1109/tmag.1978.1059918.

[25] K. O'Grady, A. Bradbury, Particle size analysis in ferrofluids, J. Magn. Magn. Mater. 39 (1) (1983/11/01/ 1983,) 91–94, https://doi.org/10.1016/0304-8853(83)90407-9.

[26] H. Pfeiffer, Determination of anisotropy field distribution in particle assemblies taking into account thermal fluctuations, phys. stat. sol. (a) 118 (1) (1990) 295–306.

[27] H. Pfeiffer, Influence of Thermal Fluctuations on the Magnetic Properties of Particle Assemblies, phys. stat. sol. (a) 122 (1) (1990) 377–389.

[28] D. Chen, J.A. Brug, R.B. Goldfarb, Demagnetizing factors for cylinders, IEEE Trans. Magn. 27 (4) (1991) 3601–3619, https://doi.org/10.1109/20.102932.

[29] D.X. Chen, E. Pardo, A. Sanchez, Fluxmetric and magnetometric demagnetizing factors for cylinders, J. Magn. Magn. Mater. 306 (1) (2006/11/01/ 2006,) 135–146, https://doi.org/10.1016/j.jmmm.2006.02.235.

[30] M.B. Stearns, Y. Cheng, Determination of para- and ferromagnetic components of magnetization and magnetoresistance of granular Co/Ag films (invited), J. Appl. Phys. 75 (10) (1994/05/15 1994,) 6894–6899, https://doi.org/10.1063/1.356773.

[31] M. Respaud, J.M. Broto, H. Rakoto, A.R. Fert, L. Thomas, B. Barbara, M. Verelst, E. Snoeck, P. Lecante, A. Mosset, J. Osuna, T.O. Ely, C. Amiens, B. Chaudret, Surface effects on the magnetic properties of ultrafine cobalt particles, Phys. Rev. B 57 (5) (1998) 2925–2935.

[32] P. Allia, M. Coisson, M. Knobel, P. Tiberto, F. Vinai, Magnetic hysteresis based on dipolar interactions in granular magnetic systems, Phys. Rev. B 60 (17) (1999) 12207–12218.

[33] P. Allia, M. Coisson, P. Tiberto, F. Vinai, M. Knobel, M. Novak, W. Nunes, Granular Cu-Co alloys as interacting superparamagnets, Phys. Rev. B 64 (14) (2001), https://doi.org/10.1103/PhysRevB.64.144420.

[34] N. Bagrets, N. Perov, A. Bagrets, A. Lermontov, G. Pankina, P. Chernavskii, Investigation of the Co particle size distribution in ensembles produced by reduction from Co oxide, J. Magn. Magn. Mater. vol. 272–276 (2004/05/01/ 2004,) 1565–1567, https://doi.org/10.1016/j.jmmm.2003.12.1272.

[35] U. Nowak, O.N. Mryasov, R. Wieser, K. Guslienko, R.W. Chantrell, Spin dynamics of magnetic nanoparticles: Beyond Brown's theory, Phys. Rev. B 72 (17) (2005), https://doi.org/10.1103/PhysRevB.72.172410.

[36] K. Mandal, S. Mitra, P.A. Kumar, Deviation from Bloch T 3/2 law in ferrite nanoparticles, Europhysics Letters (EPL) 75 (4) (2006/08 2006) 618–623, https://doi.org/10.1209/epl/i2006-10148-y.

[37] M.A. Chuev, Generalized Stoner-Wohlfarth model and the non-langevin magnetism of single-domain particles, JETP Lett. 85 (12) (2007/08/01 2007,) 611–616, https://doi.org/10.1134/S0021364007120053.

[38] M.A. Chuev, J. Hesse, Nanomagnetism: extension of the Stoner-Wohlfarth model within Néel's ideas and useful plots, J. Phys.: Condens. Matter 19 (50) (2007) 506201, https://doi.org/10.1088/0953-8984/19/50/506201.

[39] A.M. Pereira, C. Pereira, A.S. Silva, D.S. Schmool, C. Freire, J.-M. Grenèche, J. P. Araújo, Unravelling the effect of interparticle interactions and surface spin canting in γ-Fe2O3@SiO2 superparamagnetic nanoparticles, J. Appl. Phys. 109 (11) (2011) 114319, https://doi.org/10.1063/1.3583652.

[40] C. Vazquez-Vazquez, M.A. Lopez-Quintela, M.C. Bujan-Nunez, J. Rivas, Finite size and surface effects on the magnetic properties of cobalt ferrite nanoparticles, J. Nanopart. Res. 13 (4) (Apr 2011) 1663–1676, https://doi.org/10.1007/s11051-010-9920-7.

[41] M.A. Martens, R.J. Deissler, Y. Wu, L. Bauer, Z. Yao, R. Brown, M. Griswold, "Modeling the Brownian relaxation of nanoparticle ferrofluids: comparison with experiment," (in eng), Med. Phys. 40 (2) (2013) 022303, https://doi.org/10.1118/1.4773869.

[42] D.B. Reeves, J.B. Weaver, Comparisons of characteristic timescales and approximate models for Brownian magnetic nanoparticle rotations, J. Appl. Phys. 117 (23) (2015) 233905, https://doi.org/10.1063/1.4922858.

[43] M. Stier, A. Neumann, A. Kobs, H. P. Oepen, and M. Thorwart, "Generalized Neel-Brown theory for a temperature-dependent magnetic anisotropy," 2015/06/24 2015.

[44] K.L. Livesey, S. Ruta, N.R. Anderson, D. Baldomir, R.W. Chantrell, D. Serantes, Beyond the blocking model to fit nanoparticle ZFC/FC magnetisation curves, Sci. Rep. 8 (1) (2018/07/24 2018,) 11166, https://doi.org/10.1038/s41598-018-29501-8.

[45] M. Stier, A. Neumann, A. Philippi-Kobs, H.P. Oepen, M. Thorwart, Implications of a temperature-dependent magnetic anisotropy for superparamagnetic switching, J. Magn. Magn. Mater. 447 (2018/02/01/ 2018,) 96–100, https://doi.org/10.1016/j.jmmm.2017.09.068.

[46] Z. Zhao, C. Rinaldi, "Magnetization Dynamics and Energy Dissipation of Interacting Magnetic Nanoparticles in Alternating Magnetic Fields with and without a Static Bias Field," (in English), *J. Phys. Chem. C* Article 122 (36) (2018) 21018–21030, https://doi.org/10.1021/acs.jpcc.8b0407110.1021/acs.jpcc.8b04071.s00110.1021/acs.jpcc.8b04071.s00210.1021/acs.jpcc.8b04071.s00310.1021/acs.jpcc.8b04071.s00410.1021/acs.jpcc.8b04071.s00510.1021/acs.jpcc.8b04071.s00610.1021/acs.jpcc.8b04071.s007.

[47] J.A. Ramos-Guivar, A.C. Krohling, E.O. Lopez, F.J. Litterst, E.C. Passamani, "Superspinglass behavior of maghemite nanoparticles dispersed in mesoporous silica," (in English), *J. Magn. Magn. Mater.* Article 485 (Sep 2019) 142–150, https://doi.org/10.1016/j.jmmm.2019.04.067.

[48] D. Aurélio, J. Vejpravova, Understanding Magnetization Dynamics of a Magnetic Nanoparticle with a Disordered Shell Using Micromagnetic Simulations, Nanomaterials 10 (6) (2020) 1149, https://doi.org/10.3390/nano10061149.

[49] D. Zákutná, D. Nižňanský, L.C. Barnsley, E. Babcock, Z. Salhi, A. Feoktystov, D. Honecker, S. Disch, Field Dependence of Magnetic Disorder in Nanoparticles, Phys. Rev. X 10 (3) (2020), https://doi.org/10.1103/PhysRevX.10.031019.

[50] D.B. Reeves, J.B. Weaver, "Approaches for modeling magnetic nanoparticle dynamics," (in eng), Crit. Rev. Biomed. Eng. 42 (1) (2014) 85–93.

[51] S. Bedanta, W. Kleemann, Supermagnetism, J. Phys. D Appl. Phys. 42 (1) (2009) 013001, https://doi.org/10.1088/0022-3727/42/1/013001.

[52] A. Joseph, S. Mathew, "Ferrofluids: Synthetic Strategies, Stabilization, Physicochemical Features, Characterization, and Applications," (in English), *Chempluschem,* Review 79 (10) (Oct 2014) 1382–1420, https://doi.org/10.1002/cplu.201402202.

[53] M. Knobel, W.C. Nunes, L.M. Socolovsky, E. De Biasi, J.M. Vargas, J.C. Denardin, Superparamagnetism and Other Magnetic Features in Granular Materials: A Review on Ideal and Real Systems, j nanosci nanotechnol 8 (6) (2008) 2836–2857.

[54] O. Petracic, "Superparamagnetic nanoparticle ensembles," (in English), *Superlattices Microstruct.* Review 47 (5) (May 2010) 569–578, https://doi.org/10.1016/j.spmi.2010.01.009.

[55] P. E. Jonsson, "SUPERPARAMAGNETISM AND SPIN GLASS DYNAMICS OF INTERACTING MAGNETIC NANOPARTICLE SYSTEMS," (in English), *Advances in Chemical Physics, Vol 128,* Review vol. 128, pp. 191-248, 2004, doi: 10.1002/0471484237.ch3.

[56] IVO Klik, CHING.-RAY. Chang, THERMAL RELAXATION IN MAGNETIC MATERIALS: A SURVEY, SPIN 03 (02) (2013) 1330005, https://doi.org/10.1142/S2010324713300053.

[57] O. Fruchart, A. Thiaville, "Magnetism in reduced dimensions," (in English), *C.R. Phys.* Review 6 (9) (Nov 2005) 921–933, https://doi.org/10.1016/j.crhy.2005.10.011.

[58] R. Skomski, D.J. Sellmyer, in: Handbook of Advanced Magnetic Materials, Springer US, Boston, MA, 2006, pp. 1–57, https://doi.org/10.1007/1-4020-7984-2_1.

[59] M.P. Morales, et al., Surface and internal spin canting in gamma-Fe2O3 nanoparticles, Chem. Mater. 11 (11) (Nov 1999) 3058–3064, https://doi.org/10.1021/cm991018f.

[60] D.-X. Chen, A. Sanchez, E. Taboada, A. Roig, N. Sun, H.-C. Gu, Size determination of superparamagnetic nanoparticles from magnetization curve, J. Appl. Phys. 105 (8) (2009) 083924, https://doi.org/10.1063/1.3117512.

[61] S.P. Schwaminger, D. Bauer, P. Fraga-Garcia, F.E. Wagner, S. Berensmeier, "Oxidation of magnetite nanoparticles: impact on surface and crystal properties," (in English), *CrystEngComm* Article 19 (2) (Jan 2017) 246–255, https://doi.org/10.1039/c6ce02421a.

[62] V.L. Calero-Diaz del Castillo, C. Rinaldi, Effect of Sample Concentration on the Determination of the Anisotropy Constant of Magnetic Nanoparticles, IEEE Trans. Magn. 46 (3) (2010) 852–859, https://doi.org/10.1109/TMAG.2009.2032240.

[63] V.L. Calero-DdelC, C. Rinaldi, "Synthesis and magnetic characterization of cobalt-substituted ferrite (CoxFe3-xO4) nanoparticles," (in English), *J. Magn. Magn. Mater.* Article 314 (1) (Jul 2007) 60–67, https://doi.org/10.1016/j.jmmm.2006.12.030.

[64] V.L. Calero-DdelC, A.M. Gonzalez, C. Rinaldi, A Statistical Analysis to Control the Growth of Cobalt Ferrite Nanoparticles Synthesized by the Thermodecomposition Method (in English), *Journal of Manufacturing Science and Engineering-Transactions of the Asme* 132 (3) (2010), https://doi.org/10.1115/1.4001717.

[65] B. Luigjes, S.M.C. Woudenberg, R. de Groot, J.D. Meeldijk, H.M. Torres Galvis, K. P. de Jong, A.P. Philipse, B.H. Erné, Diverging Geometric and Magnetic Size Distributions of Iron Oxide Nanocrystals, J. Phys. Chem. C 115 (30) (2011) 14598–14605, https://doi.org/10.1021/jp203373f.

[66] R.M. Ferguson, A.P. Khandhar, H. Arami, L. Hua, O. Hovorka, K.M. Krishnan, Tailoring the magnetic and pharmacokinetic properties of iron oxide magnetic particle imaging tracers (in English), Biomedical Engineering-Biomedizinische Technik, Review 58 (6) (2013), https://doi.org/10.1515/bmt-2012-0058.

[67] R. Chen, M.G. Christiansen, P. Anikeeva, Maximizing Hysteretic Losses in Magnetic Ferrite Nanoparticles via Model-Driven Synthesis and Materials Optimization, ACS Nano 7 (10) (Oct 2013) 8990–9000, https://doi.org/10.1021/nn4035266.

[68] R. Hufschmid, H. Arami, R.M. Ferguson, M. Gonzales, E. Teeman, L.N. Brush, N. D. Browning, K.M. Krishnan, Synthesis of phase-pure and monodisperse iron oxide nanoparticles by thermal decomposition, Nanoscale 7 (25) (2015) 11142–11154.

[69] C. Velez, I. Torres-Díaz, L. Maldonado-Camargo, C. Rinaldi, D.P. Arnold, Magnetic Assembly and Cross-Linking of Nanoparticles for Releasable Magnetic Microstructures, ACS Nano 9 (10) (2015/10/27 2015,) 10165–10172, https://doi.org/10.1021/acsnano.5b03783.

[70] S.J. Kemp, R.M. Ferguson, A.P. Khandhar, K.M. Krishnan, Monodisperse magnetite nanoparticles with nearly ideal saturation magnetization, RSC Adv. 6 (81) (2016) 77452–77464.

[71] R. Chen, M.G. Christiansen, A. Sourakov, A. Mohr, Y. Matsumoto, S. Okada, A. Jasanoff, P. Anikeeva, "High-Performance Ferrite Nanoparticles through Nonaqueous Redox Phase Tuning," (in English), *Nano Lett.* Article 16 (2) (2016) 1345–1351, https://doi.org/10.1021/acs.nanolett.5b0476110.1021/acs.nanolett.5b04761.s001.

[72] M. Unni, A.M. Uhl, S. Savliwala, B.H. Savitzky, R. Dhavalikar, N. Garraud, D. P. Arnold, L.F. Kourkoutis, J.S. Andrew, C. Rinaldi, "Thermal Decomposition Synthesis of Iron Oxide Nanoparticles with Diminished Magnetic Dead Layer by Controlled Addition of Oxygen," (in English), ACS Nano 11 (2) (2017) 2284–2303, https://doi.org/10.1021/acsnano.7b0060910.1021/acsnano.7b00609.s001.

[73] L. Maldonado-Camargo, M. Unni, and C. Rinaldi, "Magnetic Characterization of Iron Oxide Nanoparticles for Biomedical Applications," in *Biomedical Nanotechnology: Methods and Protocols*. New York, NY: Springer New York, 2017, pp. 47-71.

[74] O.L. Lanier, O.I. Korotych, A.G. Monsalve, D. Wable, S. Savliwala, N.W. F. Grooms, C. Nacea, O.R. Tuitt, J. Dobson, Evaluation of magnetic nanoparticles for magnetic fluid hyperthermia, Int. J. Hyperth. 36 (1) (2019) 686–700, https://doi.org/10.1080/02656736.2019.1628313.

[75] M. Shliomis, "Ferrohydrodynamics: Retrospective and Issues," vol. 594, 2008, pp. 85-111.

[76] M.I. Shliomis, "Magnetic fluids," *Soviet*, Physics Uspekhi 17 (2) (1974/02/28 1974,) 153–169, https://doi.org/10.1070/pu1974v017n02abeh004332.

[77] E.C. Vreeland, J. Watt, G.B. Schober, B.G. Hance, M.J. Austin, A.D. Price, B. D. Fellows, T.C. Monson, N.S. Hudak, L. Maldonado-Camargo, A.C. Bohorquez, C. Rinaldi, D.L. Huber, "Enhanced Nanoparticle Size Control by Extending LaMer's Mechanism," (in English), *Chem. Mater.* Article 27 (17) (2015) 6059–6066, https://doi.org/10.1021/acs.chemmater.5b02510.

[78] V. Davankov, M. Tsyurupa, V. Davankov, M. Tsyurupa, Eds. *Hypercrosslinked Polymeric Networks and Adsorbing Materials* (Comprehensive Analytical Chemistry), Elsevier, USA, 2011, p. 648.

[79] R. Castaldo, G. Gentile, M. Avella, C. Carfagna, V. Ambrogi, Microporous Hyper-Crosslinked Polystyrenes and Nanocomposites with High Adsorption Properties: A Review, Polymers 9 (12) (2017) 651, https://doi.org/10.3390/polym9120651.

[80] S. Liu, A. Chiu-Lam, A. Rivera-Rodriguez, R. DeGroff, S. Savliwala, N. Sarna, C. M. Rinaldi-Ramos, Long circulating tracer tailored for magnetic particle imaging, *Nanotheranostics,* Research Paper 5 (3) (2021) 348–361, https://doi.org/10.7150/ntno.58548.

[81] E. Vreeland, Development of Novel Synthetic Methods for Size-Tunable Synthesis of Superparamagnetic Iron Oxide Nanoparticles, Engineering, University of New Mexico, Albuquerque, New Mexico, Doctor of Philosophy, 2014.

[82] C.A. Schneider, W.S. Rasband, K.W. Eliceiri, NIH Image to ImageJ: 25 years of image analysis, Nat Methods 9 (7) (2012) 671–675.

[83] C. Barrera, A.P. Herrera, N. Bezares, E. Fachini, R. Olayo-Valles, J.P. Hinestroza, C. Rinaldi, "Effect of poly(ethylene oxide)-silane graft molecular weight on the colloidal properties of iron oxide nanoparticles for biomedical applications," (in English), *J. Colloid Interface Sci.* Article 377 (1) (2012) 40–50, https://doi.org/10.1016/j.jcis.2012.03.050.

[84] B.S. Lele, M.G. Kulkarni, Single step room temperature oxidation of poly(ethylene glycol) to poly(oxyethylene)-dicarboxylic acid, Journal of Applied Polymer Science 70(5) (1998/10/31 1998) 883–890, https://doi.org/10.1002/(SICI)1097-4628(19981031)70:5<883::AID-APP7>3.0.CO;2-P.

[85] M.-Q. Zhu, E. Chang, J. Sun, R.A. Drezek, Surface modification and functionalization of semiconductor quantum dots through reactive coating of silanes in toluene, J. Mater. Chem. 17 (8) (2007) 800–805.

[86] A. Chiu-Lam, E. Staples, C.J. Pepine, C. Rinaldi, "Perfusion, cryopreservation, and nanowarming of whole hearts using colloidally stable magnetic cryopreservation agent solutions," *Science*, Advances vol. 7, no. 2 (2021) eabe3005, https://doi.org/10.1126/sciadv.abe3005.

[87] *ASTM E394-15 Standard Test Method for Iron in Trace Quantities Using the 1,10-Phenanthroline Method*, A. International, West Conshohocken, PA, 2015. [Online]. Available: https://compass.astm.org/EDIT/html_annot.cgi?E394.

[88] R.M. Cornell, U. Schwertmann, The Iron Oxides: Structure, Properties, Reactions, Wiley, Occurrences and Uses, 2006.

[89] D.M. Pajerowski, PHOTOINDUCED MAGNETISM IN NANOSTRUCTURES OF PRUSSIAN BLUE ANALOGUES, Department of Physics, University of Florida, Gainesville, Florida, Ph.D., 2010.

[90] Z. Zhao, C. Rinaldi, Computational predictions of enhanced magnetic particle imaging performance by magnetic nanoparticle chains, Phys. Med. Biol. 65 (18) (2020/09/16 2020,), 185013, https://doi.org/10.1088/1361-6560/ab95dd.

[91] J.J. Benkoski, S.E. Bowles, B.D. Korth, R.L. Jones, J.F. Douglas, A. Karim, J. Pyun, Field induced formation of mesoscopic polymer chains from functional ferromagnetic colloids, J. Am. Chem. Soc. 129 (19) (2007) 6291–6297, https://doi.org/10.1021/ja070779d.

[92] X. Qiao, M. Bai, K.e. Tao, X. Gong, R. Gu, H. Watanabe, K. Sun, J. Wu, X. Kang, Magnetorheological Behavior of Polyethyene Glycol-Coated Fe3O4 Ferrofluids, Nihon Reoroji Gakkaishi 38 (1) (2010) 23–30, https://doi.org/10.1678/rheology.38.23.

[93] G. Bertoni, B. Torre, A. Falqui, D. Fragouli, A. Athanassiou, R. Cingolani, Nanochains Formation of Superparamagnetic Nanoparticles, J. Phys. Chem. C 115 (15) (Apr 2011) 7249–7254, https://doi.org/10.1021/jp111235n.

[94] S.L. Saville, R.C. Woodward, M.J. House, A. Tokarev, J. Hammers, B. Qi, J. Shaw, M. Saunders, R.R. Varsani, T.G. St Pierre, O.T. Mefford, The effect of magnetically induced linear aggregates on proton transverse relaxation rates of aqueous suspensions of polymer coated magnetic nanoparticles, Nanoscale 5 (5) (2013) 2152–2163.

[95] S.L. Saville, B. Qi, J. Baker, R. Stone, R.E. Camley, K.L. Livesey, L. Ye, T. M. Crawford, O. Thompson Mefford, The formation of linear aggregates in magnetic hyperthermia: Implications on specific absorption rate and magnetic anisotropy, J. Colloid Interface Sci. 424 (2014) 141–151, https://doi.org/10.1016/j.jcis.2014.03.007.

[96] B. Bharti, A.L. Fameau, O.D. Velev, Magnetophoretic assembly of flexible nanoparticles/lipid microfilaments, Faraday Discuss. 181 (2015) 437–448, https://doi.org/10.1039/c4fd00272e.

[97] H. Ezzaier, J. Marins, C. Claudet, G. Hemery, O. Sandre, P. Kuzhir, Kinetics of Aggregation and Magnetic Separation of Multicore Iron Oxide Nanoparticles: Effect of the Grafted Layer Thickness, Nanomaterials 8 (8) (2018) 623, https://doi.org/10.3390/nano8080623.

[98] Z. Zhao, C. Rinaldi, Magnetization Dynamics and Energy Dissipation of Interacting Magnetic Nanoparticles in Alternating Magnetic Fields with and without a Static Bias Field, The Journal of Physical Chemistry C 122 (36) (2018) 21018–21030, https://doi.org/10.1021/acs.jpcc.8b0407110.1021/acs.jpcc.8b04071.s00110.1021/acs.jpcc.8b04071.s00210.1021/acs.jpcc.8b04071.s00310.1021/acs.jpcc.8b04071.s00410.1021/acs.jpcc.8b04071.s00510.1021/acs.jpcc.8b04071.s00610.1021/acs.jpcc.8b04071.s007.

[99] M. Agrawal, B. Rana, A. Barman, Magnetization Reversal in Chains and Clusters of Exchange-Coupled Nickel Nanoparticles, The Journal of Physical Chemistry C 114 (25) (2010/07/01 2010,) 11115–11118, https://doi.org/10.1021/jp103003a.

[100] B. Derjaguin, L. Landau, Theory of the stability of strongly charged lyophobic sols and of the adhesion of strongly charged particles in solutions of electrolytes, Prog. Surf. Sci. 43 (1) (1993/05/01/ 1993,) 30–59, https://doi.org/10.1016/0079-6816(93)90013-L.

[101] E.J.W. Verwey, Theory of the Stability of Lyophobic Colloids, The Journal of Physical and Colloid Chemistry 51 (3) (1947/03/01 1947,) 631–636, https://doi.org/10.1021/j150453a001.

[102] E. J. W. Verwey, J. T. G. Overbeek, and K. v. Nes, *Theory of the stability of lyophobic colloids; the interaction of sol particles having an electric double layer, by E. J. W. Verwey and J. Th. G. Overbeek, with the collaboration of K. van Nes*. New York: Elsevier Pub. Co., 1948.

[103] D. Grasso*, K. Subramaniam, M. Butkus, K. Strevett, J. Bergendahl, A review of non-DLVO interactions in environmental colloidal systems, Rev. Environ. Sci. Biotechnol. 1 (1) (2002) 17–38, https://doi.org/10.1023/A:1015146710500.
[104] D.L. Dorset, B. Moss, J.C. Wittmann, B. Lotz, The Pre-Melt Phase of n-alkanes: Crystallographic Evidence for a Kinked Chain Structure, PNAS 81 (6) (1984) 1913–1917.
[105] Y. Kim, H.L. Strauss, R.G. Snyder, Conformational disorder in crystalline n-alkanes prior to melting, The J of Physical Chemistry 93 (21) (1989/10/01 1989,) 7520–7526, https://doi.org/10.1021/j100358a050.